Electrochimica Acta 541 (2025) 147371



Contents lists available at ScienceDirect

Electrochimica Acta

journal homepage: www.journals.elsevier.com/electrochimica-acta





Electronic properties and ORR/OER catalytic activity of MOF-74 metal-organic frameworks: A theoretical study☆

Victor Hoyos-Sinchi, Walter Orellana *

Departamento de Física y Astronomía, Facultad de Ciencias Exactas, Universidad Andres Bello, Sazié 2212, Santiago, 8370136, Chile

ARTICLE INFO

Keywords:
Metal organic framework as electrocatalysts
Oxygen reduction reaction and oxygen evolution reaction catalytic activity
Computational hydrogen electrode method
DFT calculations

ABSTRACT

The electronic properties and catalytic activity for the oxygen reduction reaction (ORR) and oxygen evolution reaction (OER) of the metal–organic frameworks *M*-MOF-74, where *M* = Cr, Mn, Fe, Co, Ni, and Cu, were investigated using density functional theory calculations. The ORR/OER activity was assessed by evaluating the adsorption free energy of reaction intermediates on the metal centers, following the computational hydrogen electrode method. Our findings reveal that all *M*-MOF-74 structures exhibit band gap energies of approximately 2 eV and high-spin magnetic moments per metal atom with a ferromagnetic ground state. In terms of catalytic performance, Cr-MOF-74 and Fe-MOF-74 show outstanding ORR activity, with overpotentials around 0.5 V. Notably, Mn-MOF-74 and Ni-MOF-74 exhibit bifunctional ORR/OER activity, meaning they can catalyze both reactions simultaneously, with similar overpotentials of approximately 0.7 V. These ORR and OER overpotentials are comparable to those found on Pt(111) and IrO_2(110) surfaces, which are the most effective commercial electrocatalysts for the respective reactions. Additionally, the ORR/OER performance of *M*-MOF-74 is analyzed using catalytic descriptors, providing deeper insights into its electronic structure and the adsorption behavior of reaction intermediates.

1. Introduction

The oxygen reduction reaction (ORR) and oxygen evolution reaction (OER) are critical electrochemical processes that play a central role in the operation of clean energy technologies, such as hydrogen fuel cells, electrolyzers for green hydrogen production, and metal-air batteries [1–5]. Enhancing the efficiency, durability, and cost-effectiveness of these reactions is essential to fully realizing the potential of these technologies. However, in hydrogen fuel cells, the ORR at the cathode is regarded as the main limiting step in the energy conversion process due to its sluggish kinetics. Meanwhile, bifunctional ORR and OER catalysts play a crucial role in enhancing the efficiency of rechargeable metal-air batteries.

Platinum has been identified as the most efficient catalyst for the ORR. [6–9] Moreover, Pt has also been explored for the OER, alongside other metals like ruthenium and iridium, [10,11] as well as their oxides, RuO_2 and IrO_2, which have exhibited outstanding performance [12,13]. However, despite their remarkable catalytic activity, the scarcity and high cost of Ir-, Ru-, and Pt-based catalysts present major obstacles to their large-scale implementation in energy conversion technologies.

First-row transition metals, due to their natural abundance, are widely regarded as promising alternatives to noble metals in electrocatalysis for the ORR, OER, and hydrogen evolution reaction (HER). These metals are currently employed in single-atom catalysts (SACs), metal oxide catalysts, or as integral components of metal–organic frameworks (MOFs). Since Jasinski pioneering work on the ORR activity of transition-metal phthalocyanines, [14] extensive research on related coordination complexes has emerged [3,15,16]. Notably, metal cations coordinated to pyridinic nitrogen within graphitic carbon (G-MN_4) have attracted considerable interest as potential SACs for both ORR and OER. In particular, G-FeN_4 [17–20] and G-MnN_4 [21–23] have exhibited remarkable efficiency in O_2 and CO_2 reduction, approaching the catalytic performance of commercial Pt/C catalysts.

MOFs are another class of materials that have emerged as highly promising candidates in electrocatalysis for renewable energy storage and conversion, particularly in the ORR [24–26] and electrochemical water splitting OER and HER [27–29]. Among them, *M*-MOF-74, where *M* denotes a transition metal cation, stands out due to its high porosity, which forms honeycomb-like channels with exposed metal coordination sites along the pore walls. This distinctive architecture offers a large specific surface area, a crucial factor for improving electrocatalytic

☆ This article is part of a Special issue entitled: 'ITM-N-2025' published in Electrochimica Acta.

* Corresponding author.
E-mail address: worellana@unab.cl (W. Orellana).

https://doi.org/10.1016/j.electacta.2025.147371
Received 6 August 2025; Received in revised form 8 September 2025; Accepted 10 September 2025
Available online 17 September 2025
0013-4686/© 2025 Elsevier Ltd. All rights are reserved, including those for text and data mining, AI training, and similar technologies.

efficiency [30–32]. Additionally, its tunable composition enables the incorporation of various transition metals (e.g., M = Fe, Co, Ni), which have demonstrated mechanical excellent stability and outstanding OER performance in alkaline solution [33–35]. Moreover, research on the ammonia-selective catalytic reduction of NO_x using monometallic and bimetallic MOF-74 have shown that catalytic activity is strongly influenced by the choice of metal center. Specifically, Mn-MOF-74 exhibits enhanced performance due to the multiple valence states of Mn, which improve its redox properties [36]. These insights highlight the importance of further investigating ORR/OER activity and stability across different transition metals.

Despite the growing experimental interest in MOF-74 for ORR, OER, and ammonia-reduction reactions, most studies have focused on a limited set of metals, such as Fe, Co, Ni, and Cu. While these works provide valuable insights into catalytic performance, they often lack a microscopic understanding of the underlying mechanisms or the systematic dependence of activity on the electronic structure of the metal center. From a theoretical perspective, this knowledge gap remains largely unexplored. To the best of our knowledge, no prior theoretical study has systematically examined how the 3d-orbital occupation of the metal centers governs the observed activity across the first-row transition-metal series.

In this study, we investigated the electronic properties and ORR/OER catalytic activity of M-MOF-74 (M = Cr, Mn, Fe, Co, Ni, and Cu) using first-principles calculations based on density functional theory (DFT). Catalytic performance was evaluated through computed reaction overpotentials combined with descriptor analysis of the catalysts' electronic and adsorption properties [37]. Our findings indicate that all frameworks exhibit insulating properties and high-spin magnetic moments per metal atom, with a ferromagnetic ground state. Regarding catalytic performance, frameworks with M = Cr, Mn, and Fe demonstrate relatively low ORR/OER overpotentials, comparable to the best commercial catalysts, along with notable bifunctionality.

2. Computational details

Spin-polarized DFT calculations were performed using the Vienna Ab Initio Simulation Package (VASP 6.4), [38] The exchange–correlation energy was describe using the meta-GGA functional SCAN-rVV10, [39] which incorporates intermediate-range van der Waals interactions. This functional has been shown to provide a more accurate description of regions with rapidly varying electron density, such as surfaces and interfaces, as well as systems that involve both localized and delocalized electrons, which are commonly found at surfaces [40]. Additionally, Hubbard (U) corrections were incorporated to compensate for the self-interaction error among the $3d$ electrons of transition metals [41]. Our selected U values were 6.1, 5.5, 6.5, 5.3, 6.7, and 10.4 eV for Cr, Mn, Fe, Co, Ni, and Cu, respectively, following prior findings reported by Mann et al. [42] The projector augmented wave (PAW) method was used to describe the core-valence interaction [43]. In all calculations, a plane-wave cut-off energy of 425 eV was adopted, and the Brillouin zone integration was performed using a $1 \times 1 \times 2$ **k**-point mesh. Convergence tests for the cutoff energy and **k**-point grid were performed, confirming the reliability and accuracy of the chosen parameters, as shown in Figure S1. The crystalline structure of M-MOF-74 was modeled using a hexagonal unit cell containing 162 atoms, which was fully relaxed until the forces on each atom reached values below 0.025 eV/Å. The energy convergence threshold for the self-consistent field iteration was set to be 10^{-5} eV. Post-processing data and graphics were obtained using the VASPKIT [44] and VESTA [45] packages, respectively.

The ORR/OER activity of M-MOF-74 was evaluated through reaction overpotential calculations, following the computational hydrogen electrode (CHE) method introduced by Nørskov et al. [46] This approach is based on the adsorption strength of ORR/OER intermediates (OH*, O*, and OOH*) at the catalyst's active site, assessed by calculating the adsorbate free energy:

$$G_{X^*} = E_{X^*} + E_{ZPE} - TS, \tag{1}$$

where E_{X^*} is the adsorbate energy, E_{ZPE} the zero-point energy, and TS the vibrational entropic contribution. E_{ZPE} and TS were obtained from calculated vibrational frequencies of the adsorbates. In this approach, only the vibrational modes of the absorbates are explicitly considered, while the substrate is kept fixed. For gas-phase molecules, the entropy and vibrational frequencies were taken from the NIST database [47].

The adsorption free energies of the intermediates (ΔG) were calculated as the energy difference between the adsorbed species and the separate constituents, where the intermediates are expressed in terms of the stoichiometrically appropriate amounts of gas-phase H_2O and H_2, according to the equations:

$$\begin{aligned} \Delta G_{OH^*} &= G_{OH^*} - E_{MOF} + G_{1/2\,H_2} - G_{H_2O}, \\ \Delta G_{O^*} &= G_{O^*} - E_{MOF} + G_{H_2} - G_{H_2O}, \\ \Delta G_{OOH^*} &= G_{OOH^*} - E_{MOF} + G_{3/2\,H_2} - G_{2\,H_2O}, \end{aligned} \tag{2}$$

where E_{MOF} is the energy of the pristine MOF. Details of the reaction free-energy calculations can be found in Supplementary Material.

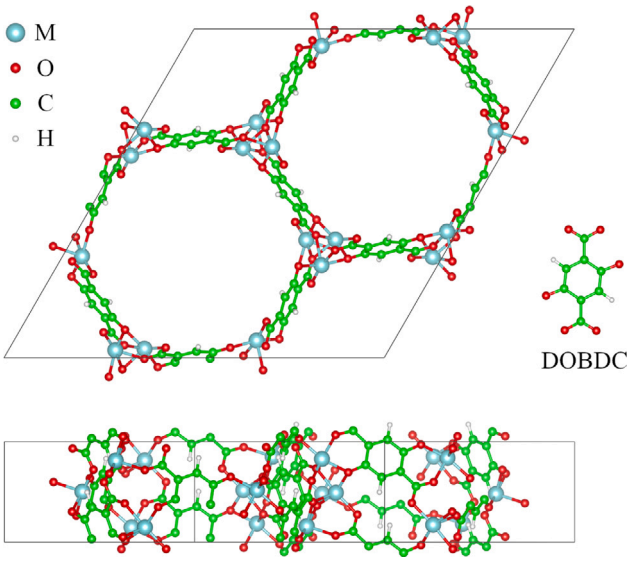

Fig. 1. Top and side view of the M-MOF-74 structure in the hexagonal unit cell representation. The metals are connected by DOBDC (2,5-dihydroxylterephthalic acid) ligands.

3. Results and discussion

3.1. Structural and electronic properties of M-MOF-74

Fig. 1 illustrates the atomic structure of M-MOF-74 in the hexagonal unit cell representation, consisting of 18 metal atoms connected by DOBDC (2,5-dihydroxyterephthalic acid) ligands. The structure features honeycomb-shaped pores with a diameter of approximately 15 Å, where the oxygen penta-coordinated M atoms expose their open metal sites to the pore channels, facilitating the interaction with incoming molecules.

Fig. 2 presents the band structure calculation of Mn-MOF-74, plotted along the high-symmetry **k**-points of the irreducible part of the Brillouin zone, together with the atomically resolved density of states (DOS). Our findings reveal nearly dispersionless bands, a characteristic feature of most MOF materials, indicating weak hybridization between

Table 1
Equilibrium lattice constants (a and c) and band gap energy at the A-point of the Brillouin zone (E_g) of M-MOF-74; m is the magnetic moment per metal atom in the unit cell.

M	a (Å)	c (Å)	E_g (eV)	m (μ_B)
Cr	25.92	6.53	1.98	4
Mn	25.98	6.88	1.68	5
Fe	25.90	6.69	1.87	4
Co	25.81	6.64	1.96	3
Ni	25.64	6.63	1.99	2
Cu	25.45	6.15	2.23	1

the ligand and metal wave functions [48]. A direct band gap of approximately 1.7 eV is identified at the A-point of the Brillouin zone, where the valence band maximum and conduction band minimum exhibit opposite spin states. Each Mn atom induces a magnetization of 5 μ_B, with ferromagnetic coupling between them, resulting in the formation of spin-polarized bands.

Similar features are observed in the band structures of the others M-MOF-74, as shown in Figure S2. Additionally, all frameworks are found to exhibit high-spin ground states, consistent with previous reports [42,49]. Table 1 summarizes the equilibrium lattice constants, band gap energies, and magnetic moments per metal atom within the unit cell for each M-MOF-74 frameworks. Experimental data for Co-MOF-74 reports a band gap energy of 2.02 eV, [50] which agree well with our calculated value of 1.96 eV. Interestingly, the total magnetic moment per M atom in M-MOF-74 matches that of an isolated M atom, suggesting that the interaction between the metal center and their nearest oxygen neighbors is predominantly ionic. This observation is further supported by the total charge and spin density distributions, as shown in Figure S3.

A recent theoretical study investigated the magnetic properties of M-MOF-74 across the 3d transition metal series after the adsorption of small molecules on the metal cation [51]. Their findings suggest that the spin configuration of the M-MOF-74 has a negligible impact on the binding strength of the adsorbed molecules.

3.2. ORR and OER catalytic activity

The ORR activity of MOF-74 is initiated by the adsorption of O_2 on the MOF metal cation. To understand this process, we first analyze the adsorption properties and equilibrium geometry of O_2 upon binding to M (O_2^*). Table 2 summarizes the binding energy, equilibrium geometry, and spin coupling of O_2 adsorbed on M-MOF-74. Our results indicate that the strength of O_2 adsorption varies significantly depending on the metal cation, with Mn, Cr, and Co displaying higher binding energies of approximately −0.4 eV. This stronger interaction correlates with an elongated O-O bond, suggesting that these metals exhibit higher reactivity toward oxygen. Interestingly, the magnetic moment of the M-MOF-74 with O_2^* changes by 0.1 μ_B compared to the pristine M-MOF-74. This observation suggests that O_2 adopts a singlet state upon adsorption, while the slight alteration in the system's magnetic moment is attributed to spin polarization effects on the MOF ligands.

Previous studies on transition-metal single-atom catalysts report that the dissociation energy of O_2^* is nearly twice that of OOH^*, [22,52] making direct O_2^* dissociation during the ORR unlikely. Instead, the reaction is expected to proceed via the sequential formation of OOH^*, O^*, and OH^* intermediates following O_2 adsorption. Fig. 3 shows the optimized geometries of these adsorbates on a Cr site in Cr-MOF-74, with similar configurations observed for the other M-MOF-74 systems. The corresponding bond lengths and angles for all M-MOF-74 structures are summarized in Table S1.

According to the CHE method, [46,53] the four-electron ORR follows these reactions:

$$O_2(g) + \mathrm{MOF} \longrightarrow O_2^*, \tag{3}$$

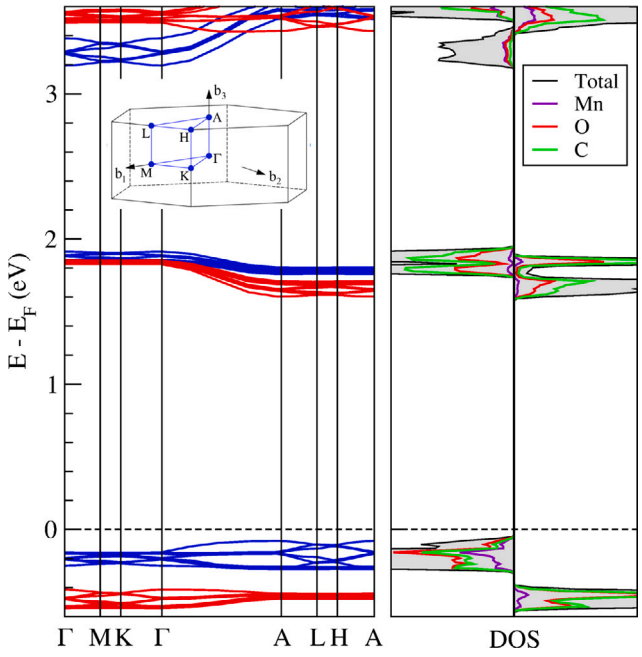

Fig. 2. Spin-polarized electronic band structure and atomic-resolved density of states (DOS) of Mn-MOF-74. The Fermi level is set at zero energy. The inset indicates high-symmetry k-points in the irreducible part of the Brillouin zone. Red and blue bands represent spin-up and spin-down, respectively.

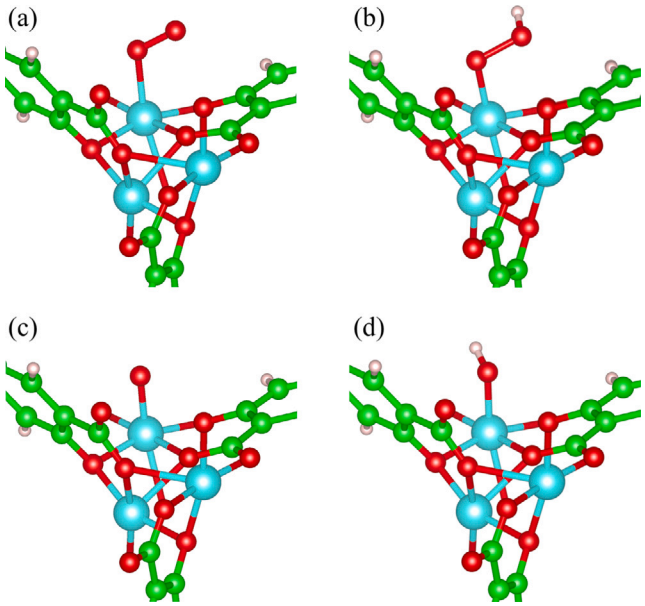

Fig. 3. Local equilibrium geometries of adsorbates on a Cr site of Cr-MOF-74. (a) O_2^*, (b) OOH^*, (c) O^*, and (d) OH^*.

$$O_2^* + H^+ + e^- \longrightarrow OOH^*, \tag{4}$$

$$OOH^* + H^+ + e^- \longrightarrow O^* + H_2O(l), \tag{5}$$

$$O^* + H^+ + e^- \longrightarrow OH^*, \tag{6}$$

$$OH^* + H^+ + e^- \longrightarrow \mathrm{MOF} + H_2O(l). \tag{7}$$

For the OER, these reactions proceed in reverse.

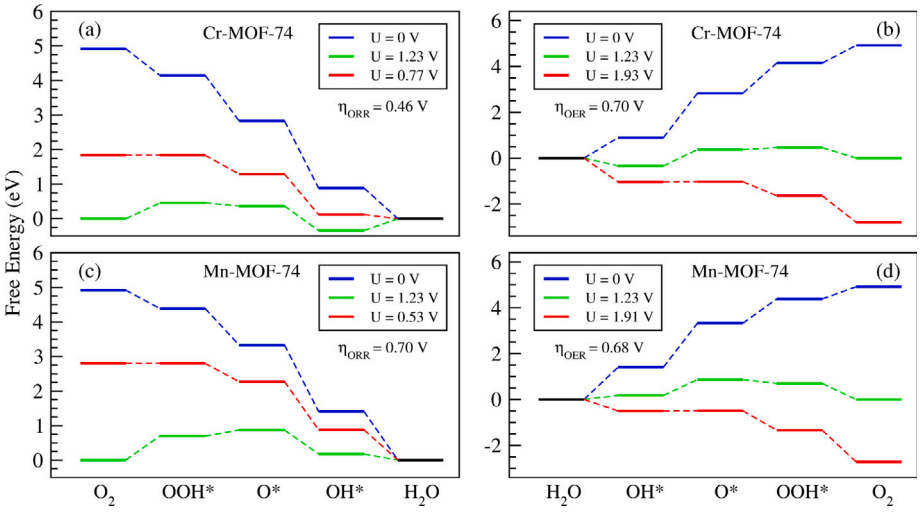

Fig. 4. Reaction free energy diagrams for the elementary steps of ORR and OER at different electrode potential (U vs RHE) for (a)–(b) Cr-MOF74 and (c)–(d) Mn-MOF74. The red free-energy diagram represents the onset potential and η the calculated overpotentials.

Table 2
Binding energy (E_b), bond length (d), and MOO angle ($\angle$) of the O_2 molecule adsorbed on the M atom of M-MOF-74; m is the magnetic moment per metal atom in the unit cell.

M–O_2	E_b (eV)	d_{M-O} (Å)	d_{O-O} (Å)	$\angle_{MOO}$ (deg)	m (μ_B)
Cr–O_2	−0.42	2.08	1.27	115	3.9
Mn–O_2	−0.45	2.14	1.26	116	4.9
Fe–O_2	−0.33	2.14	1.25	120	3.9
Co–O_2	−0.41	2.19	1.24	118	2.9
Ni–O_2	−0.33	2.19	1.25	120	2.1
Cu–O_2	−0.16	2.59	1.23	118	1.1

To evaluate the energetic of these reactions, we constructed adsorption free energy diagrams of the reaction intermediates OOH*, O*, and OH* adsorbed at the MOF's metal cation. Given the size of the MOF-74 unit cell, the shortest distance between the adsorbate and its periodic images is approximately 7 Å, ensuring no interaction between them.

The reaction steps are spontaneous at zero potential relative to the reversible hydrogen electrode (RHE) ($U = 0$ V). At the equilibrium thermodynamic potential ($U = 1.23$ V), the free energy shifts downward by the number of electrons involved in each step [54]. The potential at which all reaction steps are energetically favorable is referred to as the onset potential (U_{onset}). The theoretical overpotential (η), which quantifies ORR/OER electrocatalytic performance, is defined as the difference between the equilibrium potential and U_{onset}, namely $\eta_{ORR} = 1.23\ V - U_{onset}$ and $\eta_{OER} = U_{onset} - 1.23$ V. A detailed description of the theoretical procedure used to calculate adsorption free energy of adsorbates and ORR/OER overpotentials can be found in Supplementary Material.

An important factor to consider in electrocatalytic processes is the effect of the solvent on the adsorption free energy of intermediates, as the reactions occur in solution. Previous studies have estimated that solvent effects reduce the binding strength of OOH* and OH* on the metal center of the MN_4 complex embedded in graphene by 0.3 eV [55]. In our study, we account for solvent effects using an implicit solvent correction based on a continuum dielectric model, as implemented in VASPsol [56]. Our results show that the binding strength of OOH* and OH* on the MOF-74 metal cation decreases by 0.33 eV due to solvent correction, in good agreement with previous studies [55]. Therefore, we have incorporated this correction into the adsorption free energy calculations for these two intermediates.

Fig. 4 presents the reaction free-energy diagrams for ORR and OER activity on Cr-MOF-74 and Mn-MOF-74. Our results show that Cr-MOF-74 exhibits ORR and OER overpotentials of 0.46 and 0.70 V, respectively, as shown in Fig. 4(a) and 4(b). For Mn-MOF-74, both ORR and OER overpotentials are around 0.7 V, as shown in Fig. 4(c) and 4(d), indicating bifunctionality for this MOF. Table 3 summarizes M-MOF-74 onset potentials and overpotentials for all metal cations under study. To benchmark the catalytic performance of M-MOF-74 we reference overpotential values previously reported for the Pt(111) and IrO_2(110) surfaces, using the same theoretical model [57,58]. These surfaces are widely regarded as some of the best commercial electrocatalysts for their respective reactions. Our findings highlight the exceptional ORR catalytic activity exhibited by Cr-MOF-74 and Fe-MOF-74, comparable to that of Pt(111), as well as the outstanding OER catalytic activity exhibited by Cr-MOF-74 and Mn-MOF-74, similar to that of IrO_2(110). The free-energy diagrams for the others M-MOF-74 structures are shown in Figure S4, with detailed free-energy data provided in Tables S2 to S4. Previous theoretical studies on Fe-MOF-74 report that metal sites in the pristine structure do not promote OER [59]. Our findings are consistent with this result, as Fe-MOF-74 exhibits a relatively high OER overpotential of 0.9 V. However, for the ORR, it demonstrates good performance, with an overpotential of approximately 0.5 V.

Next, we compare our results on the catalytic performance of M-MOF-74 with predictions based on commonly reported descriptors in the literature. Fig. 5 shows the overpotential (η) as a function of the adsorbate free-energy descriptors, ΔG_{OH^*} and $\Delta G_{O^*} - \Delta G_{OH^*}$. The resulting volcano plot indicates that the lowest overpotentials correspond to M = Cr and Fe for ORR, and M = Mn, Cr, and Ni for OER. These findings are consistent with results obtained using the CHE method, confirming that these descriptors reliably capture the catalytic activity trends. Additionally, Fig. 6 shows a linear correlation between the adsorption free energies of OH* and OOH*, suggesting that the most efficient catalysts among the 3d transition metals are those exhibiting relatively weaker adsorption strengths.

Furthermore, we investigate the ORR/OER activity of M-MOF-74 using the d-band center theory, which provides insights into how the electronic structure governs catalytic reactivity across different transition metals. The d-band center (ε_d) represents the average energy of the metal d-states relative to the Fermi level and serves as a reliable descriptor for catalytic performance [60,61].

Figure S5 shows the partial density of states (PDOS) for the M(3d) orbitals in M-MOF-74. We find that ε_d lies closer to the Fermi level for Cr, Mn, and Fe, while it shifts further away for Co, Ni, and Cu. Consistently, our catalytic analysis reveals that Cr, Mn, and Fe exhibit the lowest ORR/OER overpotentials, confirming the predictive power of the d-band center model. Fig. 7 plots the overpotentials against ε_d,

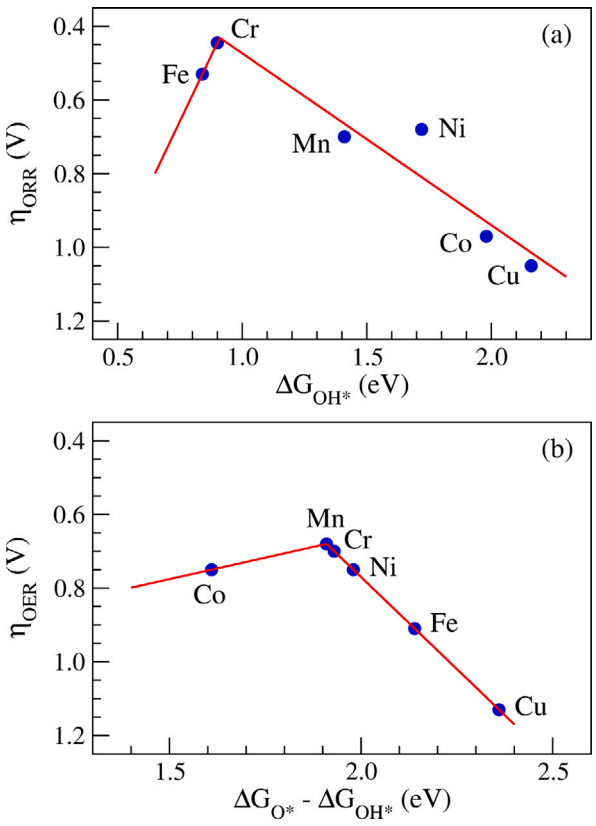

Fig. 5. Volcano plots of M-MOF-74 overpotentials (η) as a function of adsorption free energy descriptors, (a) for ORR and (b) for OER.

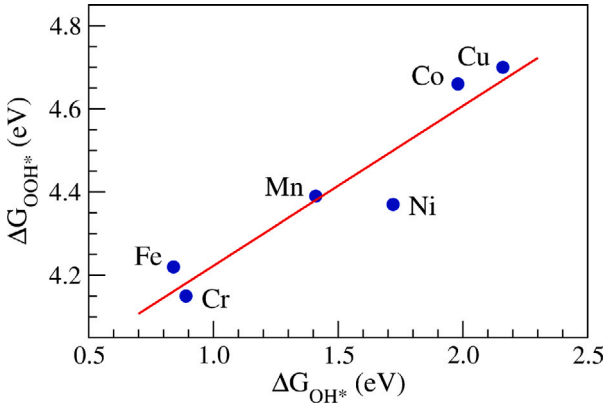

Fig. 6. Relation between adsorption free energy of OOH* and OH* intermediates.

showing a clear correlation between catalytic activity and the electronic properties of the metal centers: the most effective ORR/OER catalysts are those with ε_d values closest to the Fermi level.

We further relate the adsorption free energies of reaction intermediates to the d-band center for M-MOF-74, as shown in Figure S6. Our analysis shows that among the studied metals, Cr and Mn exhibit the highest ORR/OER activity. This behavior is attributed to their electronic configurations and d-orbital characteristics: both possess a half-filled $3d^5$ subshell, leading to high-spin states and enhanced exchange stability, which facilitate stronger hybridization with oxygen intermediates and thereby improve catalytic performance. In M-MOF-74, their ε_d values lie close to the Fermi level, yielding balanced adsorption of O*, OH*, and OOH* species. This balance optimizes the

Table 3
Theoretical results for ORR/OER onset potential (U_{onset}) and overpotential (η) for the M-MOF-74 (in V). Previous theoretical results for ORR on Pt(111) and OER on IrO_2(110) are included for comparison.

System	ORR		OER	
	U_{onset}	η	U_{onset}	η
Cr-MOF-74	0.77	0.46	1.93	0.70
Mn-MOF-74	0.53	0.70	1.91	0.68
Fe-MOF-74	0.70	0.53	2.20	0.91
Co-MOF-74	0.26	0.97	1.98	0.75
Ni-MOF-74	0.55	0.68	1.98	0.75
Cu-MOF-74	0.18	1.05	2.36	1.13
Pt(111)[a]	0.75	0.48	–	–
IrO_2(110)[b]	–	–	1.88	0.65

[a] Refs. [54].
[b] Ref. [58].

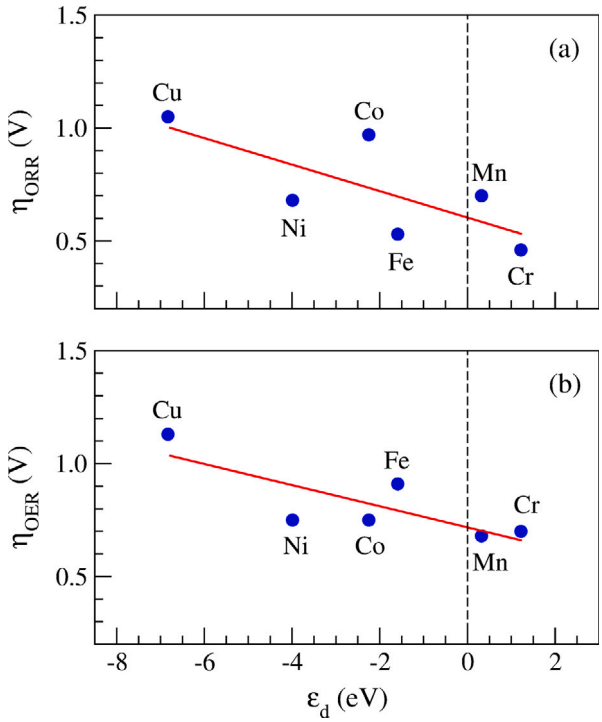

Fig. 7. ORR and OER overpotentials as a function of the d-band center (ε_d) for M-MOF-74. The dashed line indicates the Fermi energy.

reaction energetics, positioning Cr and Mn near the top of the catalytic activity volcano plots for both ORR and OER, as shown in Fig. 5.

Our findings are consistent with recent experimental studies on MOF-74 electrocatalysts. For instance, Fe-MOF-74 [34], as well as bimetallic systems such as NiFe-MOF-74 [33] and CoFe-MOF-74 [35], have demonstrated excellent OER activity in alkaline solutions, with overpotentials ranging from 0.21 to 0.28 V at 10 $mAcm^{-2}$. Additionally, Ni-MOF-74 nanosheets have shown enhanced four-electron ORR activity [31]. Interestingly, our results indicate that Fe, Ni, and Co are less active than Cr and Mn, suggesting that the latter may represent more promising candidates for future experimental investigations.

4. Summary and conclusions

In summary, we investigated the electronic properties and ORR/OER catalytic activity of the M-MOF-74 metal–organic framework (M = Cr, Mn, Fe, Co, Ni, and Cu), using spin-polarized DFT calculations. Our results indicate that all MOFs exhibit insulating properties, with

band-gap energies ranging from 1.7 to 2.2 eV. Additionally, the metals exhibit high-spin magnetization, leading to a ferromagnetic ground state in all the *M*-MOF-74 frameworks.

The ORR and OER catalytic activity was assessed through theoretical overpotentials derived from the CHE method. We found that the ORR overpotentials for Cr-MOF-74 and Fe-MOF-74 are around 0.5 V, comparable to values reported for the Pt(111) surface using a similar theoretical approach [57]. For OER, Cr-MOF-74 and Mn-MOF-74 show overpotentials of around 0.7 V, similar to those of the IrO_2(110) surface, [58] which are among the most effective commercial electrocatalysts for ORR and OER, respectively. Notably, Mn-MOF-74 and Ni-MOF-74 exhibit bifunctional ORR/OER activity, with similar overpotentials of approximately 0.7 V.

Moreover, these results are consistent with predictions based on catalytic descriptors such as the adsorption free energy and the *d*-band center. These findings deepen our understanding of structure–property relationships in MOFs and underscore their potential in electrocatalysis. Notably, our predictions of high catalytic performance and bifunctionality suggest that transition metal MOF-74 frameworks could serve as cost-effective and sustainable alternatives to noble-metal catalysts for energy conversion applications.

CRediT authorship contribution statement

Victor Hoyos-Sinchi: Writing – original draft, Visualization, Software, Methodology, Investigation, Conceptualization. **Walter Orellana:** Writing – review & editing, Supervision, Funding acquisition, Formal analysis, Conceptualization.

Declaration of competing interest

The authors declare the following financial interests/personal relationships which may be considered as potential competing interests: Walter Orellana reports financial support was provided by National Agency for Research and Development of Chile (ANID). If there are other authors, they declare that they have no known competing financial interests or personal relationships that could have appeared to influence the work reported in this paper.

Acknowledgments

We acknowledge financial support from the National Agency for Research and Development of Chile (ANID), through projects FONDECYT 1230138 and Anillo ACT 210059. V.H.-S. also thanks Universidad Andres Bello for a doctoral scholarship. The computational resources were provided by Fenix HPC (UNAB).

Appendix A. Supplementary data

Supplementary material related to this article can be found online at https://doi.org/10.1016/j.electacta.2025.147371.

Data availability

Data will be made available on request.

References

[1] M. Tahir, L. Pan, F. Idrees, X. Zhang, L. Wang, J.J. Zou, Z.L. Wang, Electrocatalytic oxygen evolution reaction for energy conversion and storage: A comprehensive review, Nano Energy 37 (2017) 136–157, http://dx.doi.org/10.1016/j.nanoen.2017.05.022.

[2] F. Chen, Z. Wu, Z. Adler, H. Wang, Stability challenges of electrocatalytic oxygen evolution reaction: From mechanistic understanding to reactor design, Joule 5 (2021) 1704–1731, http://dx.doi.org/10.1016/j.joule.2021.05.005.

[3] C.Z. Loyola, G. Abarca, S. Ureta-Zañartu, C. Aliaga, J.H. Zagal, M.T. Sougrati, F. Jaouen, W. Orellana, F. Tasca, Insights into the electronic structure of Fe penta-coordinated complexes. Spectroscopic examination and electrochemical analysis for the oxygen reduction and oxygen evolution reactions, J. Mater. Chem. A 9 (2021) 23802–23816, http://dx.doi.org/10.1039/D1TA05991B.

[4] K. Kodama, T. Nagai, A. Kuwaki, R. Jinnouchi, Y. Morimoto, Challenges in applying highly active Pt-Based nanostructured catalysts for oxygen reduction reactions to fuel cell vehicles, Nat. Nanotechnol. 16 (2021) 140–147, http://dx.doi.org/10.1038/s41565-020-00824-w.

[5] W. Zhang, W. Lai, R. Cao, Energy-related small molecule activation reactions: Oxygen reduction and hydrogen and oxygen evolution reactions catalyzed by porphyrin- and corrole-based systems, Chem. Rev. 117 (2017) 3717–3797, http://dx.doi.org/10.1021/acs.chemrev.6b00299.

[6] M. Debe, Electrocatalyst approaches and challenges for automotive fuel cells, Nature 486 (2012) 43–51, http://dx.doi.org/10.1038/nature11115.

[7] B.C.H. Steele, A. Heinzel, Materials for fuel-cell technologies, Nature 414 (2001) 345–352, http://dx.doi.org/10.1038/35104620.

[8] D. Schonvogel, J. Hülstede, P. Wagner, I. Kruusenberg, K. Tammeveski, A. Dyck, C. Agert, M. Wark, Stability of Pt nanoparticles on alternative carbon supports for oxygen reduction reaction, J. Electrochem. Soc. 164 (2017) F995–F1004, http://dx.doi.org/10.1149/2.1611709jes.

[9] S. Hussain, H. Erikson, N. Kongi, A. Sarapuu, J. Solla-Gullón, G. Maia, A.M. Kannan, N. Alonso-Vante, K. Tammeveski, Oxygen reduction reaction on nanostructured Pt-based electrocatalysts: A review, Int. J. Hydrog. Energy 45 (2020) 31775–31797, http://dx.doi.org/10.1016/j.ijhydene.2020.08.215.

[10] T. Reier, M. Oezaslan, P. Strasser, Electrocatalytic oxygen evolution reaction (OER) on Ru, Ir, and Pt catalysts: A comparative study of nanoparticles and bulk materials, ACS Catal. 2 (2012) 1765–1772, http://dx.doi.org/10.1021/cs3003098.

[11] C.C.L. McCrory, S. Jung, J.C. Peters, T.F. Jaramillo, Benchmarking heterogeneous electrocatalysts for the oxygen evolution reaction, J. Am. Chem. Soc. 135 (2013) 16977–16987, http://dx.doi.org/10.1021/ja407115p.

[12] Y. Lee, J. Suntivich, K.J. May, E.E. Perry, Y. Shao-Horn, Synthesis and activities of rutile IrO_2 and RuO_2 nanoparticles for oxygen evolution in acid and alkaline solutions, J. Phys. Chem. Lett. 3 (2012) 399–404, http://dx.doi.org/10.1021/jz2016507.

[13] S. Jung, C.C.L. McCrory, I.M. Ferrer, J.C. Peters, T.F. Jaramillo, Benchmarking nanoparticulate metal oxide electrocatalysts for the alkaline water oxidation reaction, J. Mater. Chem. A 4 (2016) 3068–3076, http://dx.doi.org/10.1039/C5TA07586F.

[14] R. Jasinski, A new fuel cell cathode catalyst, Nature 201 (1964) 1212–1213, http://dx.doi.org/10.1038/2011212a0.

[15] G. Abarca, M. Viera, C. Aliaga, J.F. Marco, W. Orellana, J.H. Zagal, F. Tasca, In search of the most active MN4 catalyst for the oxygen reduction reaction. The case of perfluorinated Fe phthalocyanine, J. Mater. Chem. A 9 (2021) 23802, http://dx.doi.org/10.1039/C9TA09125D.

[16] W. Orellana, C.Z. Loyola, J.F. Marco, F. Tasca, Evidence of Carbon-Supported porphyrins pyrolyzed for the oxygen reduction reaction keeping integrity, Sci. Rep. 12 (2022) 8072, http://dx.doi.org/10.1038/s41598-022-11820-6.

[17] M. Lefèvre, E. Proietti, F. Jaouen, J.-P. Dodelet, Iron-Based catalysts with improved oxygen reduction activity in polymer electrolyte fuel cells, Science 324 (2009) 71–74, http://dx.doi.org/10.1126/science.1170051.

[18] U. Martinez, S.K. Babu, E.F. Holby, H.T. Chung, X. Yin, P. Zelenay, Progress in the development of Fe-based PGM-free electrocatalysts for the oxygen reduction reaction, Adv. Mater. 31 (2019) 1806545, http://dx.doi.org/10.1002/adma.201806545.

[19] B. Li, S.P. Sasikala, D.H. Kim, J. Bak, I.-D. Kim, E. Cho, S.O. Kim, Fe-N_4 complex embedded free-standing carbon fabric catalysts for higher performance ORR both in alkaline and acidic media, Nano Energy 56 (2019) 524–530, http://dx.doi.org/10.1016/j.nanoen.2018.11.054.

[20] Z. Jin, P. Li, Y. Meng, Z. Fang, D. Xiao, G. Yu, Understanding the inter-site distance effect in single-atom catalysts for oxygen electroreduction, Nat. Catal. 4 (2021) 615–622, http://dx.doi.org/10.1038/s41929-021-00650-w.

[21] W. Ju, A. Bagger, G.P. Hao, A.S. Varela, I. Sinev, V. Bon, B.R. Cuenya, S. Kaskel, J. Rossmeisl, P. Strasser, Understanding activity and selectivity of metal-nitrogen-doped carbon catalysts for electrochemical reduction of CO_2, Nat. Commun. 8 (2017) 944–952, http://dx.doi.org/10.1038/s41467-017-01035-z.

[22] J. Li, M. Chen, D.A. Cullen, S. Hwang, M. Wang, B. Li, K. Liu, S. Karakalos, M. Lucero, H. Zhang, C. Lei, H. Xu, G.E. Sterbinsky, Z. Feng, D. Su, K.L. More, G. Wang, Z. Wang, G. Wu, Atomically dispersed manganese catalysts for oxygen reduction in proton-exchange membrane fuel cells, Nat. Catal. 1 (2018) 935–945, http://dx.doi.org/10.1038/s41929-018-0164-8.

[23] A.S. Varela, W. Ju, A. Bagger, P. Franco, J. Rossmeisl, P. Strasser, Electrochemical reduction of CO_2 on metal-nitrogen-doped carbon catalysts, ACS Catal. 9 (2019) 7270–7284, http://dx.doi.org/10.1021/acscatal.9b01405.

[24] F. Zheng, D. Xiang, P. Li, Z. Zhang, C. Du, Z. Zhuang, X. Li, W. Chen, Advanced electrocatalysts based on metal-organic frameworks, ACS Sustain. Chem. Eng. 7 (2019) 9743–9749, http://dx.doi.org/10.1021/acsomega.9b03295.

[25] H. Yoon, S. Lee, S. Oh, H. Park, S. Choi, M. Oh, Synthesis of bimetallic conductive 2D metal-organic framework (Co_xNi_y-CAT) and its mass production: Enhanced electrochemical oxygen reduction activity, Small 15 (2019) 1805232, http://dx.doi.org/10.1002/smll.201805232.

[26] H. Zhang, H. Osgood, X. Xie, Y. Shao, G. Wu, Engineering metal-organic framework-derived PGM-Free catalysts for oxygen reduction in acidic media, Nano Energy 31 (2017) 331–350, http://dx.doi.org/10.1149/MA2017-02/35/1508.

[27] Y. Shi, A.-F. Yang, C.-S. Cao, B. Zhao, Heterostructured MOFs photocatalysts for water splitting to produce hydrogen, Coord. Chem. Rev. 390 (2019) 50–75, http://dx.doi.org/10.1016/j.jechem.2020.10.008.

[28] X. Zheng, Y. Cao, D. Liu, M. Cai, J. Ding, X. Liu, J. Wang, W. Hu, C. Zhong, Bimetallic metal-organic-framework/reduced graphene oxide composites as bi-functional electrocatalysts for rechargeable Zn-Air batteries, ACS Appl. Mater. Interfaces 11 (2019) 15662–15669, http://dx.doi.org/10.1021/acsami.9b02859.

[29] T. Liu, P. Li, N. Yao, T. Kong, G. Cheng, S. Chen, W. Luo, Self-sacrificial template-directed vapor-phase growth of MOF assemblies and surface vulcanization for efficient water splitting, Adv. Mater. 31 (2019) 1806672, http://dx.doi.org/10.1002/adma.201806672.

[30] Z. Gao, Z.W. Yu, F.Q. Liu, Y. Y., X.M. Su, L. Wang, Z.Z. Xu, Y.L. Yang, G.R.W. andX. F. Feng, F. Luo, Ultralow-content iron-decorated Ni-MOF-74 fabricated by a metal-organic framework surface reaction for efficient electrocatalytic water oxidation, Inorg. Chem. 58 (2019) 11500–11507, http://dx.doi.org/10.1021/acs.inorgchem.9b01301.

[31] R. Fan, N. Kang, Y. Li, L. Gao, A template-directed synthesis of metal-organic framework (MOF-74) ultrathin nanosheets for oxygen reduction electrocatalysis, RSC Adv. 11 (2021) 9353–9360, http://dx.doi.org/10.1039/d0ra09973b.

[32] S.L. Rodríguez, M. Sánchez-Sánchez, J.M. Zamaro, J.L. Fernández, Understanding electron transfer processes and oxygen reduction electrocatalysis in nanocrystalline Cu-MOF-74, J. Electroanal. Chem. 918 (2022) 116489, http://dx.doi.org/10.1016/j.jelechem.2022.116489.

[33] J. Xing, K. Guo, Z. Zou, M. Cai, J. Du, C. Xu, In-situ growth of well-ordered NiFe-MOF-74 on Ni foam by Fe^{2+} induction as an efficient and stable electrocatalyst for water oxidation, Chem. Commun. 54 (2018) 7046–7049, http://dx.doi.org/10.1039/C8CC03112F.

[34] Q. Wang, F. Wei, D. Manoj, Z. Zhang, J. Xiao, X. Zhao, F. Xiao, H. Wang, S. Wang, In situ growth of Fe(II)-MOF-74 nanoarrays on nickel foam as efficient electrocatalytic electrode for water oxidation: A mechanism study on valence engineering, Chem. Commun. 55 (2019) 11307–11310, http://dx.doi.org/10.1039/C9CC05087F.

[35] X. Zhao, B. Pattengale, D. Fan, Z. Zou, Y. Zhao, J. Du, J. Huang, Xu, Mixed-node metal-organic frameworks as efficient electrocatalysts for oxygen evolution reaction, ACS Energy Lett. 3 (2018) 2520–2526, http://dx.doi.org/10.1021/acsenergylett.8b01540.

[36] S. Xie, Q. Qin, H. Liu, L. Jin, X. Wei, J. Liu, X. Liu, Y. Yao, L. Dong, B. Li, MOF-74-M (M=Mn, Co, Ni, Zn, MnCo, MnNi, and MnZn) for low-temperature NH_3-SCR and in situ DRIFTS study reaction mechanism, ACS Appl. Mater. Interfaces 12 (2020) 48476–48485, http://dx.doi.org/10.1021/acsami.0c11035.

[37] L.E.B. Lucchetti, J.M. de Almeida, S. Siahrostami, Revolutionizing ORR catalyst design through computational methodologies and materials informatics, EES Catal. 2 (2024) 1037–1058, http://dx.doi.org/10.1039/d4ey00104d.

[38] G. Kresse, J. Furthmüller, Efficient iterative schemes for Ab initio total-energy calculations using a plane-wave basis set, Phys. Rev. B 54 (1996) 11169, http://dx.doi.org/10.1103/PhysRevB.54.11169.

[39] H. Peng, Z.-H. Yang, J.P. Perdew, J. Sun, Versatile van der waals density functional based on a meta-generalized gradient approximation, Phys. Rev. X 6 (2016) 041005, http://dx.doi.org/10.1103/PhysRevX.6.041005.

[40] A. Patra, J.E. Bates, J. Sun, J.P. Perdew, Properties of real metallic surfaces: Effects of density functional semilocality and van der Waals nonlocality, Proc. Natl. Acad. Sci. USA 114 (2017) E9188–E9196, http://dx.doi.org/10.1073/pnas.1713320114.

[41] R.A. Heaton, J.G. Harrison, C.C. Lin, Self-interaction correction for density-functional theory of electronic energy bands of solids, Phys. Rev. B 28 (1983) 5992–6007, http://dx.doi.org/10.1103/PhysRevB.28.5992.

[42] G.W. Mann, K. Lee, M. Cococcioni, B. Smit, J.B. Neaton, First-principles Hubbard U approach for small molecule binding in metal-organic frameworks, J. Chem. Phys. 144 (2016) 174104, http://dx.doi.org/10.1063/1.4947240.

[43] P.E. Blöchl, Projector augmented-wave method, Phys. Rev. B 50 (1994) 17953, http://dx.doi.org/10.1103/PhysRevB.50.17953.

[44] V. Wang, N. Xu, J. Liu, G. Tang, W. Geng, VASPKIT: A user-friendly interface facilitating high-throughput computing and analysis using VASP code, Comput. Phys. Comm. 267 (2021) 108033, http://dx.doi.org/10.1016/j.cpc.2021.108033.

[45] K. Momma, F. Izumi, VESTA: A three-dimensional visualization system for electronic and structural analysis, J. Appl. Crystallogr. 41 (2008) 653–658, http://dx.doi.org/10.1107/S0021889808012016.

[46] J.K. Nørskov, J. Rossmeisl, A. Logadottir, L. Lindqvist, J.R. Kitchin, T. Bligaard, H. Jónsson, Origin of the overpotential for oxygen reduction at a fuel-cell cathode, J. Phys. Chem. B. 108 (2004) 17886–17892, http://dx.doi.org/10.1021/jp047349j.

[47] National Institute of Standard and Technology, 2024. https://www.nist.gov.

[48] W. Orellana, Metal substitutions in the MOF-5 metal-organic framework: A hybrid density functional theory study, J. Phys. Chem. C 128 (2024) 6471–6477, http://dx.doi.org/10.1021/acs.jpcc.4c00944.

[49] K. Lee, J.D. Howe, L.-C. Lin, B. Smit, J.B. Neaton, Small-molecule adsorption in open-site metal-organic frameworks: A systematic density functional theory study for rational design, Chem. Mat. 27 (2015) 668–678, http://dx.doi.org/10.1021/cm502760q.

[50] J.A. Botas, G. Callejas, M. Sánchez-Sánchez, M.G. Orcajo, Effect of Zn/Co ratio in MOF-74 type materials containing exposed metal sites on their hydrogen adsorption behaviour and on their band gap energy, Int. J. Hydrog. Energy 36 (2011) 10834–10844, http://dx.doi.org/10.1016/j.ijhydene.2011.05.187.

[51] N. Jodaeeasl, S. Wang, A. Hu, G.H. Peslherbe, Comprehensive DFT investigation of small-molecule adsorption on the paradigm M-MOF-74 family of metal-organic frameworks, Phys. Chem. Chem. Phys 27 (2025) 3068, http://dx.doi.org/10.1039/d4cp02873b.

[52] W. Orellana, R.H. Miwa, Fe and Co adatoms on bilayer borophene as single-atom catalysts for the oxygen reduction reaction: A theoretical study, Phys. Rev. Appl. 21 (2024) 034008, http://dx.doi.org/10.1103/PhysRevApplied.21.034008.

[53] F. Calle-Vallejo, J.I. Martínez, J.M. García-Lastra, E. Abad, M.T.M. Koper, Oxygen reduction and evolution at single-metal active sites: Comparison between functionalized graphitic materials and protoporphyrins, Surf. Sc. 607 (2013) 47–53, http://dx.doi.org/10.1016/j.susc.2012.08.005.

[54] A. Kulkarni, S. Siahrostami, A. Patel, J.K. Nørskov, Understanding catalytic activity trends in the oxygen reduction reaction, Chem. Rev. 118 (2018) 2302, http://dx.doi.org/10.1021/acs.chemrev.7b00488.

[55] F. Calle-Vallejo, J.I. Martinez, J. Rossmeisl, Density functional studies of functionalized graphitic materials with late transition metals for oxygen reduction reactions, Phys. Chem. Chem. Phys. 13 (2011) 15639, http://dx.doi.org/10.1039/c1cp21228a.

[56] K. Mathew, R. Sundararaman, K. Letchworthweaver, T.A. Arias, R.G. Hennig, Implicit solvation model for density-functional study of nanocrystal surfaces and reaction pathways, J. Chem. Phys. 140 (2014) 084106, http://dx.doi.org/10.1063/1.4865107.

[57] H.A. Hansen, J. Rossmeisl, J.K. Nørskov, Surface pourbaix diagrams and oxygen reduction activity of Pt, Ag and Ni(111) surfaces studied by DFT, Phys. Chem. Chem. Phys 10 (2008) 3722–3730, http://dx.doi.org/10.1039/B803956A.

[58] H. Xu, D. Cheng, D. Cao, X.C. Zeng, A universal principle for a rational design of single-atom electrocatalysts, Nat. Catal. 1 (2018) 339–348, http://dx.doi.org/10.1038/s41929-018-0063-z.

[59] J. Morales-Vidal, R. García-Muelas, M.A. Ortuño, Defects as catalytic sites for the oxygen evolution reaction in earth-abundant MOF-74 revealed by DFT, Catal. Sci. Technol. 11 (2021) 1443–1450, http://dx.doi.org/10.1039/d0cy02163f.

[60] B. Hammer, J.K. Nørskov, Why gold is the noblest of all the metals, Nature 376 (1995) 238–240, http://dx.doi.org/10.1038/376238a0.

[61] B. Hammer, J.K. Nørskov, Theoretical surface science and catalysis–calculations and concepts, Adv. Catal. 45 (2000) 71–129, http://dx.doi.org/10.1016/S0360-0564(02)45013-4.